HAL open science

Why fumed and precipitated silica have different mechanical behavior: Contribution of discrete element simulations

E. Guesnet, B. Bénane, D. Jauffres, C.L. Martin, G.P. Baeza, G. Foray, S. Meille, C. Olagnon, B. Yrieix

To cite this version:

E. Guesnet, B. Bénane, D. Jauffres, C.L. Martin, G.P. Baeza, et al.. Why fumed and precipitated silica have different mechanical behavior: Contribution of discrete element simulations. Journal of Non-Crystalline Solids, 2019, 524, pp.119646. 10.1016/j.jnoncrysol.2019.119646 . hal-02352818

HAL Id: hal-02352818

https://hal.science/hal-02352818v1

Submitted on 20 Dec 2021

HAL is a multi-disciplinary open access archive for the deposit and dissemination of scientific research documents, whether they are published or not. The documents may come from teaching and research institutions in France or abroad, or from public or private research centers.

L'archive ouverte pluridisciplinaire **HAL**, est destinée au dépôt et à la diffusion de documents scientifiques de niveau recherche, publiés ou non, émanant des établissements d'enseignement et de recherche français ou étrangers, des laboratoires publics ou privés.

Distributed under a Creative Commons Attribution - NonCommercial 4.0 International License

Version of Record: https://www.sciencedirect.com/science/article/pii/S0022309319305174
Manuscript_13961834b80daf1ecb06b37a0214596d

Why fumed and precipitated silica have different mechanical behavior: contribution of discrete element simulations

E. Guesnet[a], B. Bénane[b], D. Jauffrès[a], C. L. Martin[a], G. P. Baeza[b], G. Foray[b], S. Meille[b], C. Olagnon[b], B. Yrieix[c]

[a] *Univ. Grenoble Alpes, CNRS, Grenoble INP, SIMaP, F-38000 Grenoble, France*
[b] *Univ Lyon, INSA-Lyon, Université Claude Bernard Lyon 1, CNRS UMR-5510, MATEIS, 7, Avenue Jean Capelle, 69621 Villeurbanne Cedex, France.*
[c] *EDF R&D site des Renardières, Écuelles, 77818 Moret-sur-Loing Cedex*

Abstract

Precipitated silica (PS) could be an interesting alternative to fumed silica (FS) for the core of Vacuum Insulation Panels (VIP), in particular to reduce their cost and widen their use. However, compacted PS exhibits, for the same density, lower mechanical properties than FS. A better understanding of the mechanical behavior of these materials would help to design PS with optimized mechanical properties for VIP. In this work, complemented with experimental characterization, Discrete Element Method (DEM) simulations are used to investigate the compaction behavior and post-compaction tensile behavior of a set of numerically generated silica aggregates with varying neck size, surface energy and morphology (primary particle size, fractal dimension and gyration radius). During the compaction stage, neck size has the largest influence on the mechanical behavior, whereas during the tensile stage the influence of surface energy predominates. These results should be taken with caution as the task of modeling such a complex system necessarily involves

© 2019 published by Elsevier. This manuscript is made available under the CC BY NC user license
https://creativecommons.org/licenses/by-nc/4.0/

bias due to simplifying assumptions. However, it is believed that the experimentally observed differences between PS and FS in compaction behavior and strength may lie not only in aggregates morphological differences, but also in different surface energies and neck sizes.
Keywords: Discrete Element Method, Vacuum Insulation Panels, powder compaction, nanostructured silica, fractal aggregates

---

1. Introduction

Energy consumption to heat or cool buildings is an important contributor to greenhouse gas emission and leads to other environmental damages. Efficient insulation can largely contribute to reduce the amount of energy required. While in many countries new constructions are low-energy ones thanks to regulations imposing efficient insulation, old buildings are often badly insulated and need to be retrofitted. Thermal retrofitting of housing is an important lever for the reduction of greenhouse gas emissions.

A wide range of retrofitting materials and techniques exists on the market, the most commons being mineral wool and expanded polystyrene foam. Their thermal conductivity varies between $\lambda = 30$ to 35 mW/(m.K) for a cost of 10 to 15€/m^2 (for a thermal resistance $R_T = 3$ m^{2}K/W). For the same insulation performance, a larger thickness is required for materials with higher thermal conductivity. While having a thick layer is generally not too detrimental for insulation from the outside, insulation from the inside is often required (outside space shortage, conservation of the original historical facade) and thick insulation layer is in this case a barrier to thermal retrofitting.

Thin panel for insulation from the inside can only be achieved with super-

insulation materials ($\lambda < 25$ mW/(m.K)). The most mature super-insulation technology, Vacuum Insulation Panels (VIP), consists of a highly porous nanostructured silica core wrapped under vacuum (pressure ≤ 5 mbar) inside a sealed envelope [1, 2, 3]. VIP cost is high (> 100€/m^2 [4]), mainly because of the nanostructured silica core, but thermal conductivities as low as 5 mW/(m.K) are reached. Even if a cost analysis including the saved floor area makes VIP an economically viable choice in high housing price areas [4, 5], their high initial cost is detrimental for their wider use. The nanostructured nature of the silica core is essential in VIP as it allows the reduction of thermal conductivity by the Knudsen effect [6, 7], which leads to significantly longer service life than non-nanostructured materials such as glass fibers [4]. The use of precipitated silica (PS) in place of fumed (also called pyrogenic) silica (FS) as nanostructured core material would significantly reduce the cost of VIP [2]. Precipitated silica is indeed a widely available material, in particular because of its use as a filler in the tire industry [8]. Also, because of its production by a low temperature process, PS may help to decrease the embodied energy of VIP [9]. Indeed, FS is obtained from an energy consuming high temperature (> 1200 °C) pyrolysis of silicon tetrachloride. Primary particles of 7 to 50 nm in diameter form in flame and coalesce in stable aggregates [10]. Polydispersity in primary particle size arises from temperature gradients in flame and has been observed within a single aggregate by Transmission Electron Microscopy (TEM) [11]. The aggregates have a fractal morphology [11, 12] with a fractal dimension that may vary depending on the flame temperature and other process parameters. Aggregates also exhibit a polydispersity in size as shown by Small Angle X-ray

Scattering (SAXS) [11]. The silica surface is made of both silanol groups (Si-OH) and siloxane bridges (Si-O-Si) leading to an intermediate hydrophilic character [13]. PS are obtained via acid or base precipitation in an aqueous solution of silicates, resulting in a more hydrophilic surface with a high density of silanol groups. The primary particle size is slightly larger than for FS [14] and the fractal dimension is also generally larger than for FS [8, 15]. Aggregates of FS and PS form at a larger scale agglomerates (few hundred nanometers) and then powder grains at the macroscale (few microns). However, the mechanical properties of VIP core made of precipitated silica appear very limited. It has been shown for example that to reach a compressive strength of 100 kPa (considered as a minimum required for handling and vacuuming), PS has to be compacted to at least 220 kg/m^3 versus 160 kg/m^3 for FS [2]. A recent study by instrumented indentation confirms the lower mechanical properties of PS compacts with indentation modulus half as low for PS as for FS for a similar apparent density [16]. Thermal conductivity greatly depends on the core material density hence the need of a larger compaction density, or the addition of reinforcing fibers, for PS core degrades strongly thermal properties. In short, the thermal/mechanical compromise is presently not optimal to allow the replacement of FS by PS.

Fumed and precipitated silica are nonetheless very similar materials and the origin of the observed differences in mechanical behavior is not clear. It has been suggested that the aspect ratio of the aggregates and their capacity to entangle influence the mechanical behavior [16]. Differences in surface chemistry and primary particle size also play a role [17]. Last, the influence of ageing should also be considered. While the influence of ageing on the ther-

mal properties and the service life time has been studied [7, 13], the effect of ageing on mechanical properties has been less investigated. A better understanding of the mechanical behavior in relation with aggregate morphology and surface chemistry would be highly valuable to improve the mechanical properties of precipitated silica. Conversely to FS and PS compacts, the mechanical behavior of silica aerogels have been extensively studied through both experiments and modeling [18, 19, 20, 21, 22, 23, 24]. In particular, the necklace structure of primary particles have motivated mesoscale modeling using the Discrete Element Method (DEM) [20] and coarse-grained molecular dynamics [21]. Also, the significant impact of surface energy on mechanics in these nanostructured highly porous materials has been demonstrated by molecular dynamics [22].

In this work, a better understanding of the peculiar contrasted mechanical behavior of FS and PS is sought based on macroscale experimental mechanical characterization and mesoscale DEM modeling. In particular, the use of DEM allows independent assessment of the influence of various morphological or material parameters such as fractal dimension, primary particle size, aggregate size, neck size and surface energy. The paper is organized as follows. First, the mechanical behaviour of FS and PS is investigated experimentally during oedometric compaction to confirm and measure the differences between both silica. Experiments will also be used for comparison with modeling. The modeling approach and the contact laws are detailed in section 3. The generation of realistic numerical samples, based on recent morphological characterization of the nanostructured silica [11, 25], is described in section 4. Results are presented in section 5 and discussed in section 6.

2. Experimental characterization

2.1. Materials and methods

A commercial FS (Konasil 200, OCI, Korea) and two commercial PS (Tixosil 365 & Tixosil 43, Solvay, France) have been investigated. While the FS silica has a hydrophobic character (1 to 2.5 OH/nm^2[26, 27, 28]), the PS silicas are highly hydrophilic (4 to 16 OH/nm^2 [27, 29]). The intrinsic (skeletal) densities reported by the manufacturers are 2200 kg/m^3 for the FS and 2100 kg/m^3 for the PS. Oedometric compression tests were performed with a 20 mm diameter cylindrical die using a sapphire pellet in contact with the powder to ensure a flat surface. The same initial mass of powder was used for the three silicas. A conventional testing machine (Zwick-Roell, Germany) was used and the displacement of the punch was recorded with a LVDT sensor. The crosshead speed was 10 mm/min during loading and 5 mm/min during unloading. The same maximum force (400 N, leading to a maximum pressure of 1.27 MPa) was used for all powders. This value was chosen to obtain final pellets with a density close to what is required for the final application (i.e. 200 kg/m^3 for FS [3]). It must also be mentioned that the silica powder compaction behavior is highly sensitive to humidity and temperature during the test. The conditions of the tests were similar in terms of relative humidity (35% to 45%) and temperature (20°C to 24°C) between the three silicas.

2.2. Results

The initial relative densities (volume fractions of solid) after pouring the powder in the die were ca. 3% for Konasil 200, and 7.5% for T365 and T43

silica powders. This simple observation already demonstrates significant differences between FS and PS, the former having a significantly lower initial relative density. The compaction curves (average over several tests) are displayed in Fig. 1. A significant difference in compaction behavior of FS and PS is observed, with the FS being significantly harder to compact. The final densities reached after a 1.27 MPa compaction are ca. 290 kg/m^3($\approx$ 13%) for PS compacts versus ca. 210 kg/m^3($\approx$ 10%) for FS compacts. The oedometric elastic modulus has also been assessed during the first 10% of unloading: 22.4 $\pm$ 0.5 MPa, 17.5 $\pm$ 1.0 MPa and 18.7 $\pm$ 1.0 MPa for Konasil 200, Tixosil 43 and Tixosil 365 respectively. These values are not directly comparable as the difference in density at 1.27 MPa is large between FS and PS. Still, it is remarkable that even at a significantly lower density the FS compact is stiffer than the PS one. Directly comparable data was obtained from iso-density compaction of the three powders to ca. 10%. Compaction pressure and oedometric modulus at 10% density are reported in Table 1 and confirm that FS compacts are significantly stiffer than PS ones. These results are consistent with a recent instrumented indentation study showing that, for a similar density of compacts ca. 10%, FS is twice stiffer than PS [16]. The measurement of tensile strength of the compacted silica pellets is a challenging task. Still, preliminary biaxial flexural test have shown that for a density of 200 kg/m^3 PS exhibits extremely low strength ($<$ 0.1 MPa), 3 to 5 times lower than FS (ca. 0.3 MPa) at the same density .These results confirm the contrasting behavior between the two types of nanostructured silica.

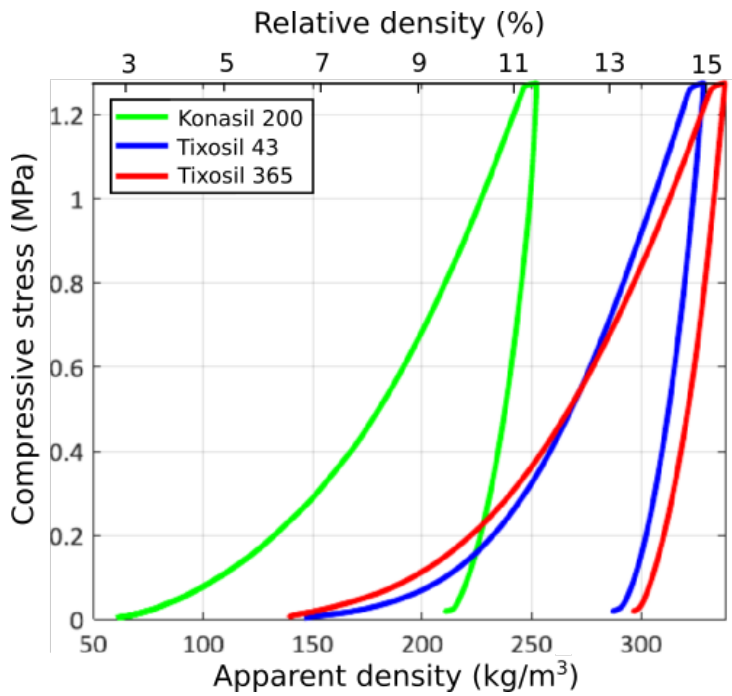

Figure 1: Compaction behavior of fumed (Konasil 200) and precipitated (Tixosil 365 & Tixosil 43) silica. The relative density has been computed based on an intrinsic density of 2200 kg/m^3

	Compaction pressure (MPa)	Apparent density (kg/m^3)	Relative density (%)	Oedometric modulus (MPa)
Konasil 200	0.64	218 ± 2	9.9 ± 0.1	10.4 ± 0.2
Tixosil 43	0.16	198 ± 2	9.5 ± 0.1	2.9 ± 0.2
Tixosil 365	0.16	200 ± 2	9.5 ± 0.1	3.7 ± 0.2

Table 1: Comparison of oedometric modulus of compacts at iso-density

3. Model description

3.1. Discrete Element Method framework

The classical DEM approach [30] is used with Hertzian and bonded contacts [31]. In DEM the dynamic motion of discrete entities (generally spherical particles) is computed by an explicit time integration of the second law of Newton. Each particle transmit forces to its neighbors through their contacts. The open source version of LIGGGHTS ®[32] was used with our own implementation of bonded contacts and numerical damping. For post-processing and visualization OVITO [33] was used. In short, at each time step, the DEM algorithm is as follows:

- for each particle a neighbor (or contact) list is established;
- for each contact, forces (and resisting moments) are computed according to contact laws;
- forces (and moments) are summed for each particle;
- Newton's second law and time integration (Velocity-Verlet) are used to get the new particle position.

The mechanical loading is performed by changing the size of the simulation box in one or more directions according to a prescribed strain rate. All particles are moved according to the corresponding affine displacement at the beginning of the timestep. In the present work a quasi-static approach is sought by using low enough strain rates. The quasi-static strain rate is reached once further decrease in strain rate does not affect significantly the results. In order to dissipate the kinetic energy in the system and damp

oscillations, viscous forces and moments are added. They oppose the contact normal displacements and rotations. Following the work of Agnolin and Roux [34], the damping coefficient was chosen as a fraction $\beta = 0.1$ of the critical damping coefficient. A non-viscous damping force, that opposes the particle velocity and proportional (with a coefficient $\alpha = 0.7$) to the total force acting on the particle, is also applied to each particle [30]. The macroscopic stress tensor on the simulation box of volume V is computed as follows [35]:

$$\sigma_{ij} = \frac{1}{V} \sum_{contacs} F_i l_j \tag{1}$$

where F_i is the ith component of the contact force vector, and l_j is the jth component of the branch vector connecting the centers of the two particles in contact. The reader will find more details on the DEM method in the following works: [30, 31, 32, 34, 36, 37]. Here we will only focus on the description of the contact laws.

3.2. Contact laws

Two types of contacts are distinguished: bonded contacts that can transmit normal and tangential forces and resisting moments [31], and Hertzian contacts with Derjaguin-Muller-Toporov (DMT) adhesion [38]. Initially, all intra-aggregates contacts are bonded. New contacts appearing during the simulation are then considered as Hertzian. The latter are mainly inter-aggregate contacts but Hertzian contacts may also appear within an aggregate during its compaction if initially close (but not bonded) particles of an aggregate contact each other.

The contact law proposed by Jefferson et al. [39] and Jauffres et al. [40], to model the elastic behavior of a solid neck between two sintered particles,

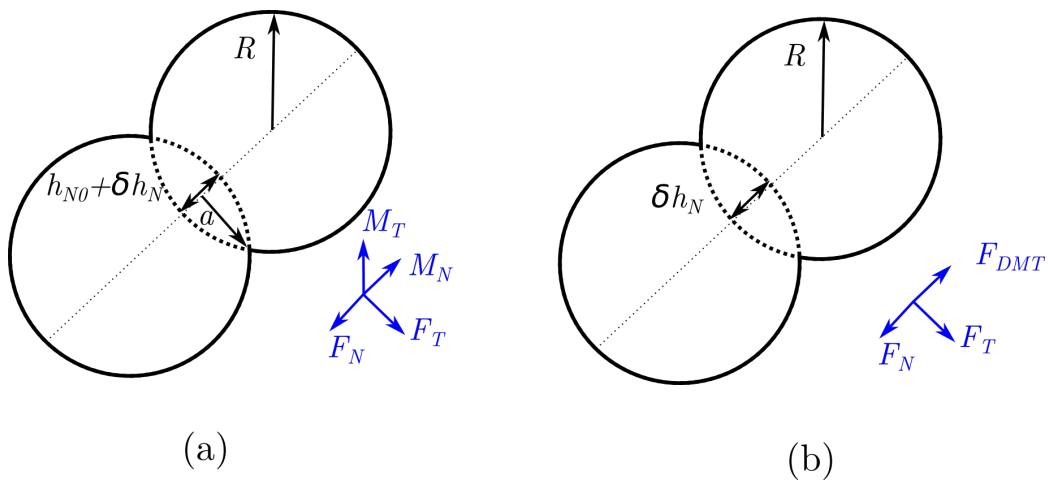

Figure 2: Contact laws. (a) bonded contact. (b) Hertzian contact

is used for bonded contacts. This model has been successfully used for silica aerogels by Liu et al. [20]. It is given here for a monomodal set of particles of radius R but has been also developed for particles with different radii [40].

Normal force F_N, tangential force F_T, resisting bending M_T and twisting moments M_N (Fig. 2) are given as a function of the contact size a and the elastic properties of the particles, i.e., the Young's Modulus E and the Poisson's ratio ν:

$$F_N = k_N \delta h_N,\ k_N = \frac{E}{1-\nu^2} f_N a \tag{2}$$

$$F_T = k_T \delta h_T,\ k_T = \frac{2E}{(2-\nu)(1+\nu)} f_T a \tag{3}$$

$$M_N = k_{MN} \alpha_N,\ k_{MN} = \frac{a^2 k_T}{2} \tag{4}$$

$$M_T = k_{MT} \alpha_T,\ k_{MT} = \frac{a^2 k_N}{4} \tag{5}$$

where k_N, k_T, k_{MN} and k_{MT} are stiffnesses; δh_N and δh_T are the normal relative displacement and tangent accumulated displacement; α_N and α_T are

the accumulated relative rotations. The coefficients f_N and f_T have been obtained from finite element simulations at the scale of one sintered neck by McMeeking et al. [41]:

$$f_N = \frac{1 + a^* \left(\frac{\pi}{6}(1-\nu^2)(1+2a^*) - a^*\right)}{\sqrt{1-(a^*)^2} - \frac{c_0+4c_1}{\pi}\left(a^* + (a^*)^2\left(\frac{\pi}{6}(1-\nu^2)(1+2a^*) - a^*\right)\right)} \tag{6}$$

$$f_T = \frac{1 + (a^*)^2 \left(\frac{\pi}{6}(1-\nu^2)(1+2a^*) - a^*\right)}{\sqrt{1-(a^*)^2}} \tag{7}$$

with

$$a^* = \frac{a}{R} \tag{8}$$

$$c_0 = 0.5650 + 0.04864\nu^2 + 1.036\nu^4 \tag{9}$$

$$c_1 = 0.1396 - 0.03061\nu + 0.3395\nu^2 \tag{10}$$

Typical elastic properties of dense amorphous silica were used: $E = 70$ GPa and $\nu = 0.2$. Equations (4) and (5) are derived from beam theory [31]. Practically, the linear stiffness coefficients k_N, k_T, k_{MN} and k_{MT} are computed according to a given contact size a in a pre-processing step. The same contact size a is used for all bonded contacts. For the sake of simplicity, and also because aggregates are generally considered as unbreakables, no explicit fracture criteria is used. Still, if the normal force is such that the distance between two particles become larger than twice their radius the bond will disappear leading to a geometric breakage of the bond. To limit this artificial behavior an initial overlap h_{N0} (Fig. 2) is used between the particles as detailed in section 4.1.1.

Newly formed contacts during simulation are of Hertzian type with Coulomb friction and DMT adhesion [38]:

$$F_N = \frac{\sqrt{2R}}{3} \frac{E}{1-\nu^2} \left(\delta h_N\right)^{1.5} \tag{11}$$

$$F_T = \min\left(\frac{E\sqrt{2R}}{(2-\nu)(1+\nu)} \sqrt{\delta h_N} \delta h_T, \mu F_N\right) \tag{12}$$

$$F_{DMT} = -2\gamma_S \pi R \tag{13}$$

with μ the friction coefficient, γ_S the surface energy (J/m^2). F_{DMT} is an attractive force normal to the contact that adds up to the repulsive Hertzian force F_N. A simple dimensional analysis on Eq. (1) shows that the only force that introduces a size effect is the DMT adhesion (Eq. (13)) as it introduces a term with an inverse size dependence ($1/R$) in the macroscopic stress σ_{ij}. It is also worth noting that while during synthesis or ageing surface energy and particle size are correlated, these two parameters can be set independently in the DEM simulations.

4. Simulation methods

4.1. Numerical preparation of initial silica powder bed

4.1.1. Initial gas with controlled aggregate morphology

The porous Eden growth model [42] was used to generate aggregates, i.e. random assemblies of spherical primary particles in contact. The porous Eden model allows the generation of aggregates with a controlled morphology through two parameters: the number of particles N and the inactivation probability P. The random inactivation of particles with the probability

P allows the local blocking of the growth to create porous structures. Aggregates are successively generated inside a periodic (in all three directions) simulation box to form an initial gas of aggregates. When attempting to place a new particle, the non-overlapping condition applies within the growing aggregate and with the other aggregates already in the simulation box. Experimentally observed initial density (3% for FS and 7.5% for PS) are sufficiently low to ensure that no significant bias exists in the generation of aggregates due to this globally applied non-overlapping condition. In addition, the particle radii are multiplied by a factor ξ to create overlapping contacts (required to limit the geometric breakages) which introduces a third generation parameter. It is important to underline the model nature of the gas of aggregates numerically generated: perfect spheres are used, large scale organization (agglomerate, powder particle) is not considered and no dispersion is used on the particle radius. The fractal dimension and gyration radius are not generation parameters: they are computed after the aggregate generation as described in [42]. Briefly, the gyration radius is computed using the classical definition $R_g = \frac{1}{N}\sqrt{\sum_{i,j>i}^{N}(r_{ij})^2}$, where r_{ij} is the distance between particles i and j, and the fractal dimension is obtained through the slope of the structure factor versus q (modulus of the scattering vector) plot. Consequently there is a small dispersion on these two aggregate characteristics, inherent to the random nature of the generation procedure. As the two selected PS (Tixosil 43 & 365) have a quite similar mechanical response under oedometric compaction, only Konasil 200 and Tixosil 365 silica were studied numerically. Their fractal dimension d_f, aggregate gyration radius R_g and primary particle radius R were obtained from SAXS [11, 25]. Their

	SAXS [11, 25]			Numerical					
	d_f	R_g	R	d_f	R_g	R	N	P	ξ
Konasil 200 (FS)	2.0	64	7	2.0	64	8.3	133	61 %	1.3
Tixosil 365 (PS)	> 2.4	35	13	2.4	38	12	35	0 %	1.3

Table 2: Morphological properties (fractal dimension d_f and radius of gyration R_g) and generation parameters (particle radius R, number of particles per aggregate N, inactivation probability P and radius increase factor ξ) of numerically generated aggregates. The radius R reported is after enlargement by the factor ξ. R_g and R are in nanometers. Morphological properties from SAXS experiment used as input to the optimization algorithm are also reported. While a meticulous extraction of d_f from aggregates dispersed in a very low volume fraction suspension was possible for FS [11], the d_f value used for PS may be overestimated due to aggregate interaction [25].

numerical counterparts were generated using an optimization algorithm as described in [42]. Morphological properties used as inputs and the numerical parameters resulting from the optimization are reported in Table 2. Images of typical aggregates are provided in Fig. 3 (see also supplementary videos). In total, 30,000 particles, leading to a gas of at least 200 aggregates and a simulation box of $\approx 1\ \mu\text{m}^3$ (vs. a few mm^3 for the experiment), were used to ensure a good reproducibility during the subsequent mechanical simulations.

4.1.2. Sample preparation by compression-tension cycling

Performing directly a compression of the low density gas of aggregate to simulate the experimental odeometric compaction is not realistic. Indeed, starting with an initial gas, by definition with no inter-aggregates contacts, do not correspond to the experimental initial aggregate packing for which silica aggregates exhibit contacts. We noted several anomalies during the

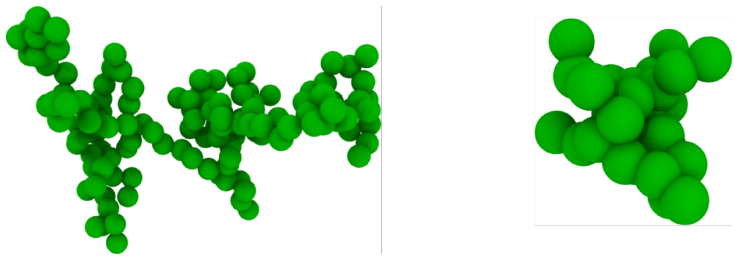

Figure 3: Typical aggregates numerically generated based on SAXS morphological characterization. Left: Konasil 200 (FS), primary particle radius $R = 8.3$ nm. Right: Tixosil 365 (PS), primary particle radius $R = 12$ nm. Note that the enlargement of the particles by the factor ξ has created overlaps

compaction of a gas of aggregates that might be related to this unrealistic initial state:

- large amount of geometric bond breakages (5%),
- still increasing number of Hertzian contacts during tensile loading,
- underestimation of the stresses (ca. 0.3 MPa vs 1.2 MPa in experiment).

A procedure to create more realistic initial packings has been developed based on compression-tension cycling at low density. Packing by gravitation might be a possible alternative but with the drawback of breaking the periodic boundary condition in at least one direction. From a given initial gas, 8 uniaxial compression-tension cycles of amplitude 0.025 (i.e. from 3% to 5.5% for FS) are performed to create Hertzian inter-aggregate contacts. Creation of new contacts due to adhesive forces and rearrangement occurs during the cycling, leading to a more realistic initial state. The number of cycle has been limited to 8 as more cycles lead to a large amount of unwanted geometrical

bond breakages. 8 cycles also corresponds to the threshold from which the number of Hertzian contacts start decreasing during the tensile loading stage (Fig. 4). Fig. 5 shows that after cycling, although a fully continuous network is not achieved, large structures of several aggregates linked by adhesion are formed. To maximize the rearrangements and creation of Hertzian contacts, the friction coefficient has been set to 0 and surface energy to 1.2 J/m^2 for this preparation stage. The other contact law parameters are the same than in the subsequent simulation of compaction and tensile tests. It should be noted that to keep reasonable CPU time, the strain rate has been increased by a factor 10 above the quasi-static strain rate for the preparation stage. This is not problematic considering the fact that the preparation procedure is purely numerical and does not seek to reproduce the material behavior.

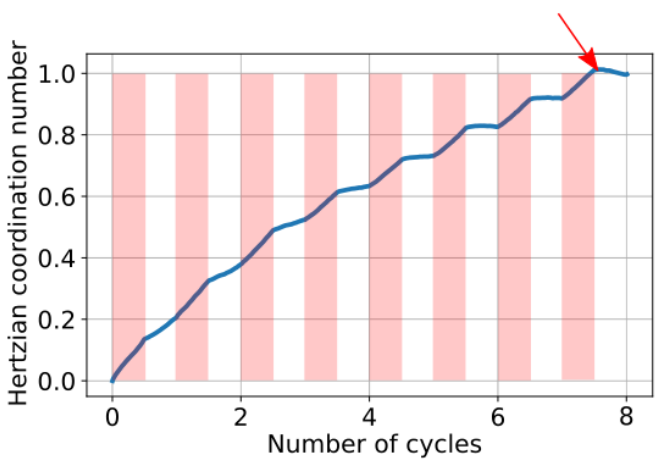

Figure 4: Evolution of the Hertzian coordination number (i.e. the average number of Hertzian contacts per particle) with compression-tension cycling during sample preparation. The compression stages are indicated in red. The Hertzian coordination increases both during compression and tension, until the last cycle where it decreases during tension (red arrow).

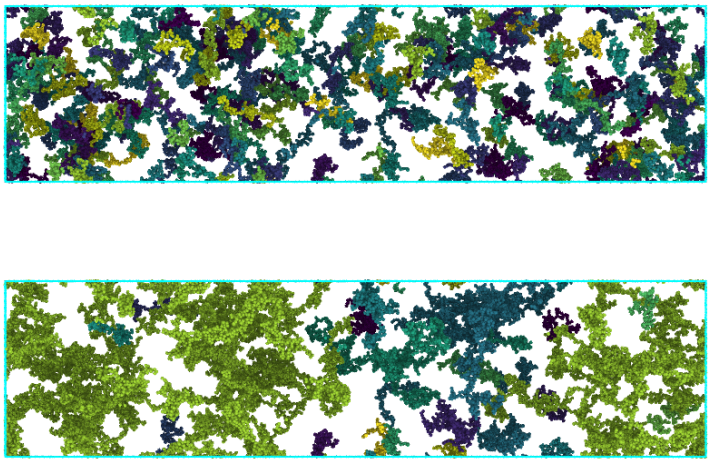

Figure 5: Influence of cycling. (top) No cycling, a different color is assigned to each aggregate indicating that each aggregate is isolated. (bottom) After 8 cycles, colors show the class of equivalence of contacting aggregates indicating a large number of inter-aggregate contacts. The relative density is 3% for both and only a slice of the simulation box is shown.

4.2. Compaction of a silica powder bed to VIP core density followed by tensile test

First, a uniaxial compaction is performed up to a given nominal density and then a uniaxial tensile loading is imposed in the same direction. Five simulations on different initial gas of aggregates were run for each set of parameters to provide an error bar. A typical stress-density curve is reported in Fig. 6. For the sake of clarity the compressive and tensile parts will be reported in two separate graphs. The state of the initial assembly of aggregates (in particular the number of Hertzian contacts) affects the result but primarily the beginning of the compaction and only moderately the maxi-

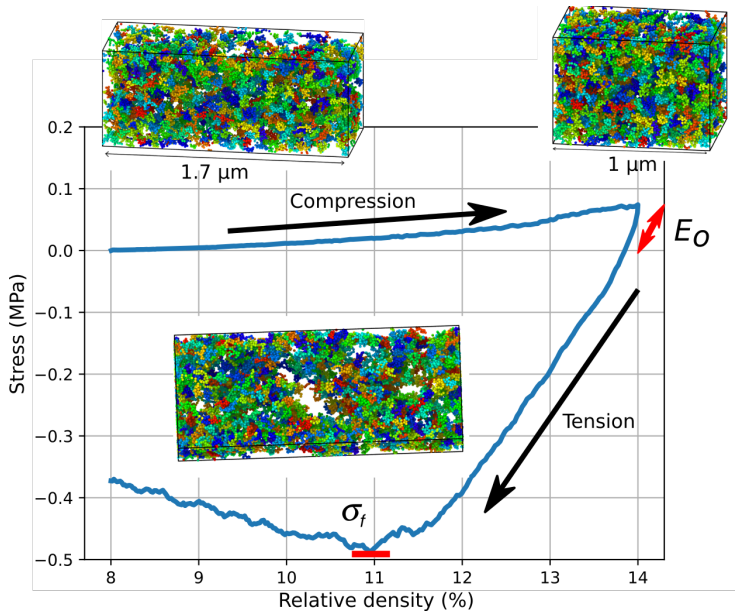

Figure 6: Typical simulation: compaction of a silica powder bed to VIP core density followed by a tensile test. Odoemetric modulus E_0 and strength σ_f are extracted from the simulation to characterize the mechanical behavior of the silica core produced by the compaction stage.

mum stress and tension stage. In the extreme case of no hertzian contacts (no cycling during the preparation stage) the maximum compressive stress is ca. 25 % lower than for 8 cycles during the preparation stage (1 Hertzian contact per particle). The oedometric modulus E_o is computed during the first 0.5% of unloading. During the tensile loading, a maximum tensile stress σ_f is reached and will be defined as the material strength. The fracture is progressive and does not exhibit any sudden drop in stress. We identified two main reasons for this non-brittle behavior. First and as observed in MD [24, 22] or DEM simulations [20], surface energy plays a predominant role in the mechanics of these materials with large surface to volume ratio and nano-

metric particles. The adhesive forces (modelled here with the DMT model, Eq. (13)) that appear when aggregates resume contact do not allow for a brittle failure. Second, when dealing with small scale simulation, no large defect of micron size that may lead to a catastrophic failure at the macro scale is included in the modeling. The strength values may thus be overestimated for this reason but are still relevant for relative comparison of various silica types. It is also worth noting that in this system, the adhesive DMT forces have a significant influence on the compressive behavior. For example, even during compaction, the Hertzian contacts maintain an attractive character ($F_N + F_{DMT} < 0$) and thus contribute negatively to the macroscopic compressive stress.

5. Results

5.1. Influence of contact law parameters

The stiffness of the bonded contacts between two particles in the aggregates depends, apart from the Young's modulus of the particle, on the contact size a (Eq. (11)), a parameter difficult to assess, even with TEM images [14]. Liu et al. have assessed the ratio $\frac{a}{R}$ in a silica aerogel by considering, during gelation, neck formation by Johnson-Kendall-Roberts (JKR) adhesion [43]. This approach would also be applicable for PS and interestingly leads to $\frac{a}{R} = 0.26$ for a primary particle of radius 13 nm (value reported for PS, Table 2). It is also worth noting that $\frac{a}{R}$ is expected to increase with ageing of the material [7, 13]. In this work we used $\frac{a}{R} = 0.3$ as a rough estimate and performed a parametric study around this value for FS aggregates (morphological parameters in Table 2 with surface energy $\gamma_s = 1.2$ J/m^2

and friction coefficient $\mu = 0.3$). The compaction stress-density curves and tensile stress-strain curves are reported in Fig. 7. As expected increasing $\frac{a}{R}$ leads to a stiffer aggregate packing due to an increase of the stiffness of the aggregates. The behavior is highly non-linear with a relatively low increase of the maximum compressive stress between $\frac{a}{R} = 0.15$ and $\frac{a}{R} = 0.3$ and a much larger one between $\frac{a}{R} = 0.3$ and $\frac{a}{R} = 0.6$. This comment also holds for the oedometric modulus that takes the values $E_0 = 5.8$, 8.8 and 21.0 MPa for $\frac{a}{R} = 0.15$, 0.3 and 0.6, respectively. The tensile strength also increases with the contact size as the aggregates becomes stiffer, even if the number of newly formed Hertzian contacts is lower (rearrangement of stiff aggregates is more difficult).

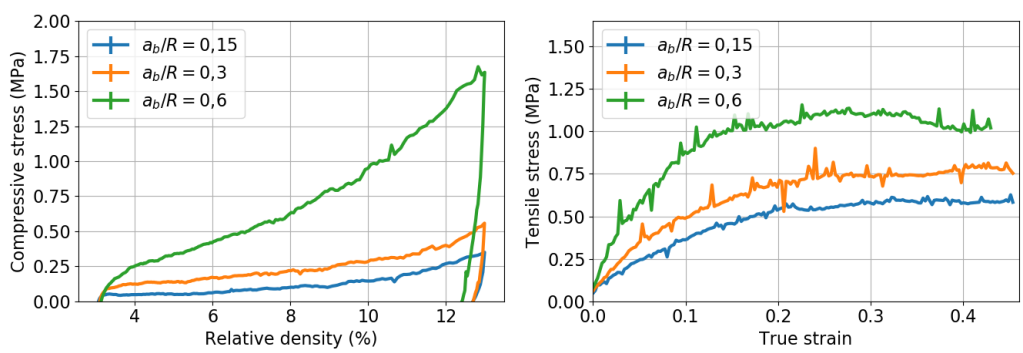

Figure 7: Influence of contact size on the compaction behavior (left) and the tensile behavior (right). FS aggregates with $\gamma_s = 1.2$ J/m^2 and $\mu = 0.3$. Averaging is done over 5 timesteps and 5 simulations, relative standard deviation $\leq 10\%$.

Moreover, the behavior of Hertzian contacts is largely dependant on the value of surface energy γ_s. 1 J/m^2 is generally considered as a good estimate for oxides [44]. A surface energy of approximately 1 J/m^2 has been calculated by MD simulations for pure Silica [45]. However, in the case of

silica, the chemical nature of the surface (density of silanol groups and physically adsorbed water), that depends on the processing route (pyrogenic or in aqueous solution), the degree of ageing and the relative humidity [7, 13, 46], plays an important role. Indeed, chemically or physically adsorbed water can screen Van der Waals and electrostatics interactions in favor of capillary forces leading to a lower surface energy [47]. In consequence silica surface energy varies from 5 J/m^2 in ultradry conditions [48] to 0.1 J/m^2 for pure capillary interaction [47]. To assess the influence of surface energy, a parametric study on γ_s was performed for FS aggregates with $\frac{a}{R} = 0.3$ and $\mu = 0.3$. The results in Fig. 8 show that γ_s has a relatively low impact on the compaction behavior but a significant influence on the strength and oedometric modulus ($E_0 = 2.5$, 6.7 and 8.8 MPa for $\gamma_s = 0$, 0.4 and 1.2 J/m^2, respectively). Values larger than 1.2 J/m^2 are not reported as the amount of unrealistic geometrical bond breakages become non-negligible and may impact the macroscopic result.

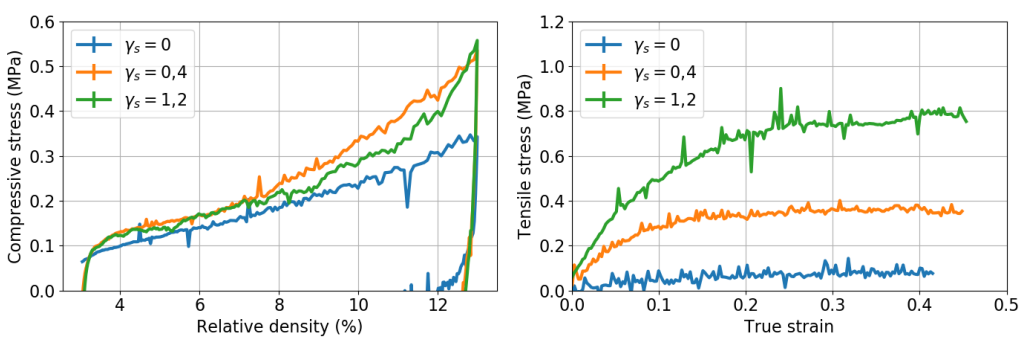

Figure 8: Influence of surface energy on the compaction behavior (left) and the tensile behavior (right). FS aggregates with $\frac{a}{R} = 0.3$ and $\mu = 0.3$. Averaging is done over 5 timesteps and 5 simulations, relative standard deviation $\leq 10\%$.

No statistically significant influence of the friction coefficient varying from $\mu = 0.1$ to 0.9 has been noted, but simulations with $\mu = 0$ exhibit significantly lower compaction stresses. The negligible effect of μ might sounds surprising but is a consequence of very adhesive hertzian contacts. Indeed, the indentation is very large ($\delta h_N/R \approx 0.1$) because of the adhesive forces and consequently F_T is, even with $\mu = 0.1$, very rarely capped by μF_N ($F_N \propto {\delta h_N}^{1.5}$ and $F_T \propto {\delta h_N}^{0.5}$ see equations 11 and 12), which explains the very limited influence of μ.

5.2. Influence of aggregate morphology

The influence of the morphological parameters of aggregates has been studied with the following values for the contact law parameters: $\gamma_s = 1.2\ \mathrm{J/m^2}$, $\frac{a}{R} = 0.3$ and $\mu = 0.3$. The parametric study has been performed around the values of FS aggregates (Table 2). In such a nano-sized system, adhesive interaction are of outmost importance and are directly linked to the size of particles (equation (13)). Keeping other parameters identical and enlarging only the primary particle radius up to a value typical of PS has nearly no influence on the compaction behavior but decreases the strength (Fig. 9). This is consistent with the parametric study on γ_s: varying the primary particle or the surface energy affects similarly the DMT adhesion forces (Eq. (13)).

FS aggregates are generally more branched and elongated than PS, which is quantified by a smaller fractal dimension d_f [8, 11, 42] (Fig. 10). When the initial density (set by the compression-tension preparation stage) and the gyration radius are kept constant, the fractal dimension of the aggregates shows only a limited effect on the compaction behavior, oedometric modulus and strength for d_f varying from 1.7 to 2.8 (Fig. 11). It is worth noting that the

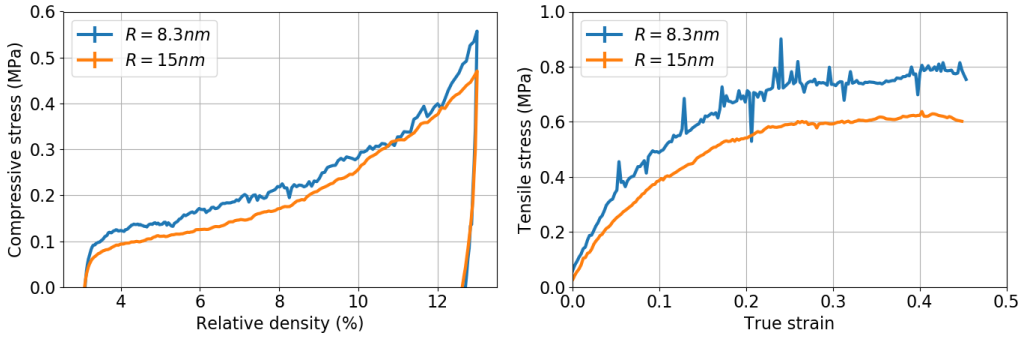

Figure 9: Influence of primary particle radius on the compaction behavior (left) and the tensile behavior (right). $\gamma_s = 1.2$ J/m^2, $\frac{a}{R} = 0.3$, $\mu = 0.3$. Averaging is done over 5 timesteps and 5 simulations, relative standard deviation $\leq 10\%$.

number of Hertzian contacts formed during the compression-tension preparation stage is larger with low d_f as more elongated and branched aggregates tend to interpenetrate each other more than rounded aggregates. During the compaction stage, it is also noted that samples with low d_f form more new Hertzians contacts than samples with high d_f.

Lastly, the influence of the gyration radius is investigated. Fig. 12 displays typical aggregates with increasing radius of gyration used in the simulation. d_f is kept constant but because of the increasing number of particles the aggregates are more elongated with large R_g for the porous Eden growth model [42]. It is observed in Fig. 13 that the compaction is more difficult for large R_g values. The oedometric modulus follows the same trend than the compaction stress and increases with R_g ($E_0 = 6.3$, 8.8 and 9.1 MPa for $R_g = 30$, 64 and 128 nm, respectively). Strength is nearly unaffected by R_g (Fig. 13).

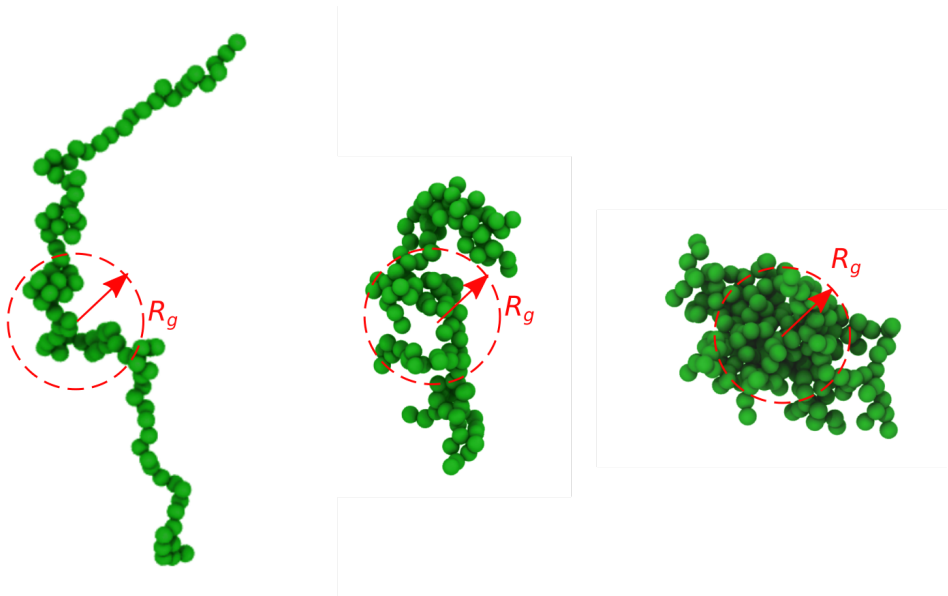

Figure 10: Aggregates with increasing fractal dimension d_f at constant radius of gyration $R_g = 64$ nm . From left to right $d_f = 1.7$, $d_f = 2.0$ and $d_f = 2.8$. Aggregates with larger d_f have a larger number of primary particles to keep R_g constant [42].

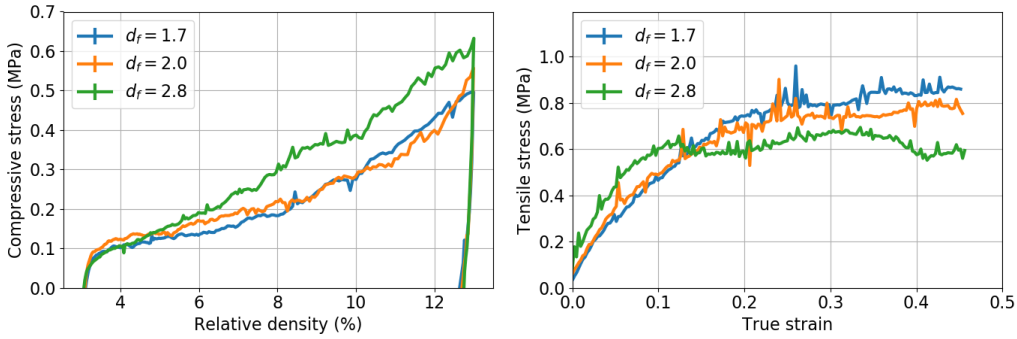

Figure 11: Influence of aggregate fractal dimension on the compaction behavior (left) and the tensile behavior (right). $\gamma_s = 1.2$ J/m^2, $\frac{a}{R} = 0.3$, $\mu = 0.3$. Averaging is done over 5 timesteps and 5 simulations, relative standard deviation $\leq 15\%$.

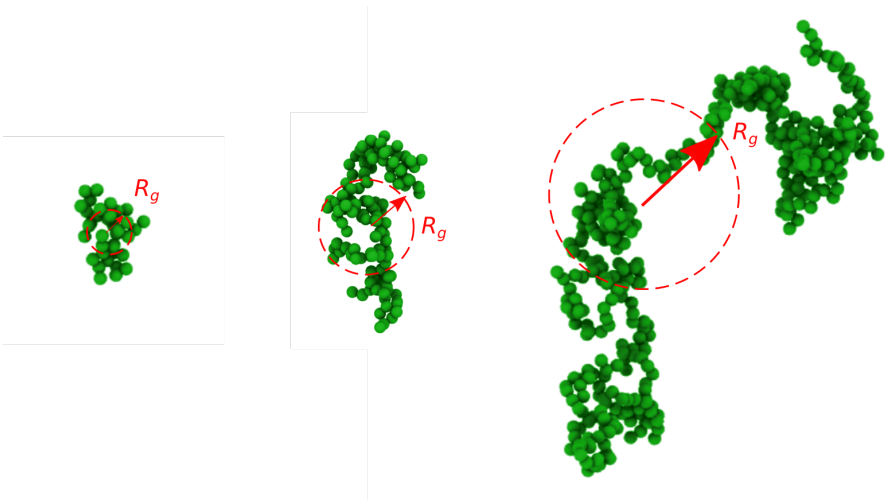

Figure 12: Aggregates with increasing radius of gyration R_g at constant $d_f = 2.0$. From left to right $R_g = 30$ nm, $R_g = 64$ nm and $R_g = 128$ nm. Aggregates with larger R_g are more elongated [42].

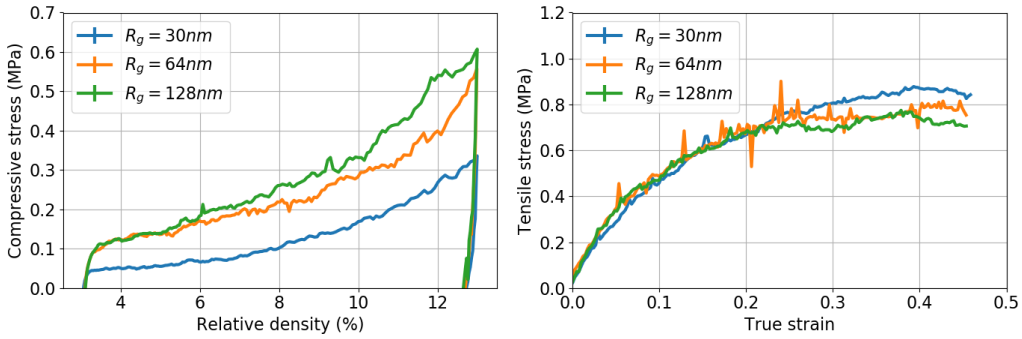

Figure 13: Influence of aggregate radius of gyration on the compaction behavior (left) and the tensile behavior (right). $\gamma_s = 1.2$ J/m^2, $\frac{a}{R} = 0.3$, $\mu = 0.3$. Averaging is done over 5 timesteps and 5 simulations, relative standard deviation $\leq 21\%$, 5% and 13% for $R_g = 30$, 64 and 128 nm respectively.

5.3. Comparison with experiment

For the sake of comparison with the experimental study reported in section 2, compaction and tensile behavior of numerically generated FS and PS

were simulated. In the absence of reliable assessments of the surface energy and the neck size, the same values were used for FS and PS ($\gamma_s = 1.2$ J/m^2 and $\frac{a}{R} = 0.3$). The experimentally observed initial relative densities were targeted during the initial sample preparation by compression-tension cycling. To follow the experiment, the final density of PS was set to a larger value than the FS one. Compaction curves and tensile stress-strain curves are reported in Fig. 14. Qualitatively the initial part of the compaction curves is very steep, which is not observed experimentally. However, we believe this is an artifact due to the non quasi-staticity of the compression-tension cycling, that may lead to a system slightly out of equilibrium at the beginning of the compaction. Quantitatively, the simulation compressive stresses are lower than the experimentally observed ones but the order of magnitude is correct. This is satisfactory considering the fact that no parameter has been fitted and that neck size, which has a tremendous effect on the stress (Fig. 7), has only been very roughly estimated and fixed constant for all the particles. The fact that the simulations underestimate the compressive stresses suggests however that the actual neck size maybe larger than the one estimated from JKR model. The simulation odeometric moduli (8.8 MPa for FS at 13 % and 14.5 MPa for PS at 17 %) are lower than the experimentally measured values at lower densities (22.4 MPa for FS at 11 % and 18.7 MPa for PS at 15 %) but the correct order of magnitude is also obtained. For the fracture behavior, only a rough experimental estimation of the strength is known, and again the order of magnitude is correct, at least for FS (ca. 0.3 MPa at a density of 9 % experimentally versus 0.75 MPa but at a density of 13 % numerically). As for PS, the difference in density (9 % experimentally versus

17 % numerically) makes the comparison difficult. The fact that PS has a larger oedometric modulus and strength than FS is difficult to interpret due also to the large difference in density of the two compacts.

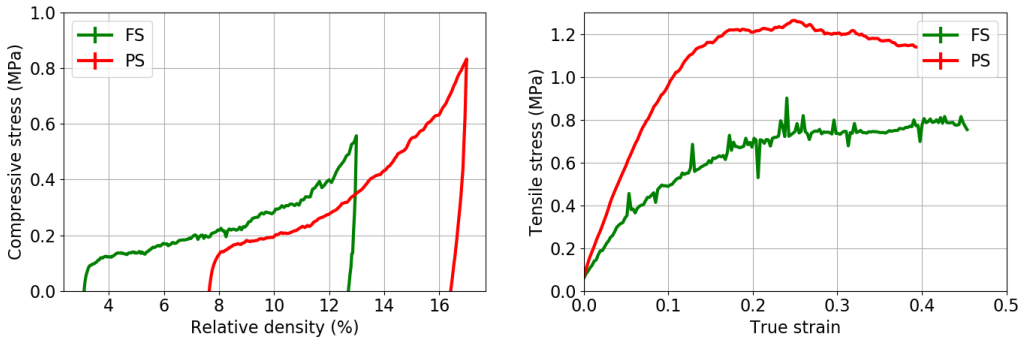

Figure 14: Comparison of the compaction behavior (left) and the tensile behavior (right) of fumed (K200) and precipitated (T365) silica powders. Averaging is done over 5 timesteps and 5 simulations, relative standard deviation $\leq 10\%$.

5.4. Scaling law for oedometric modulus

In order to compare the two silica over similar density range, unloading steps during the compaction were used to evaluate the oedometric modulus of the packing versus its density. The results are reported in log-log plot in Fig. 15, showing that at similar density FS is stiffer than PS but only by a small amount, ca. 20%. The data follow a scaling law of the form $E_0 \propto d^{\kappa}$. The computed exponents of the scaling have intermediate values between what is expected for an open foam structure ($\kappa = 2.0$ [49]) and a silica hydrophobized aerogel ($\kappa = 3.8$ [22]).

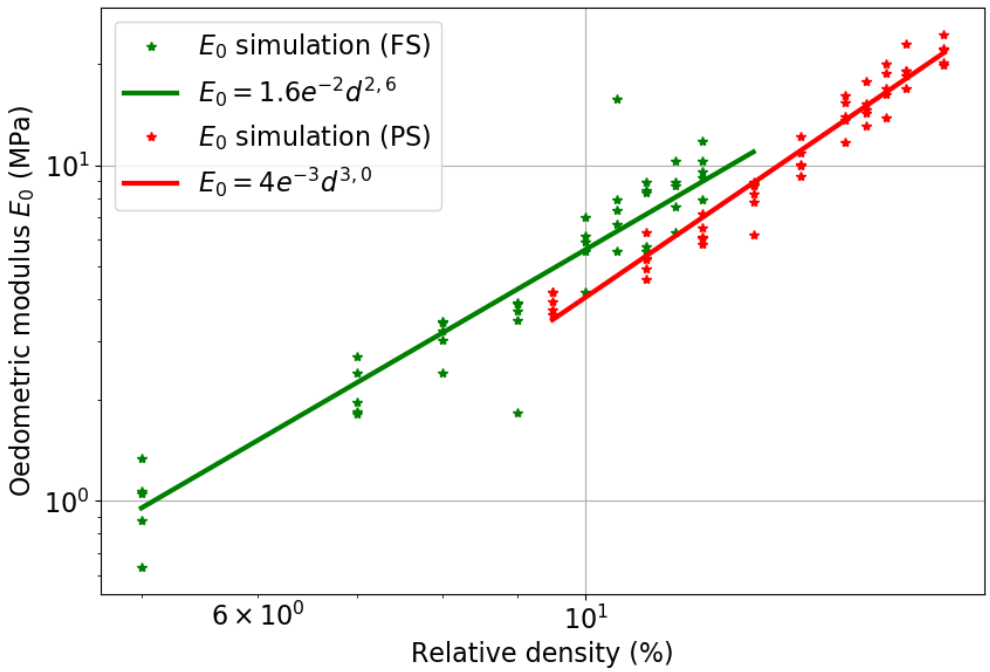

Figure 15: Scaling law between oedometric modulus E_0 and relative density d for PS and FS.

6. Discussion

The parameters governing the mechanical behavior in compaction of nanostructured silica powders in the simulations are, by increasing order of significance:

- neck size between bonded primary particles
- gyration radius of the aggregate
- surface energy (or primary particle radius)

The fact that the fractal dimension has very limited influence appears surprising as more elongated and branched aggregates have been suggested as a possible explanation for the observed stronger mechanical behavior under compaction and indentation of FS powders [16]. First, the elongation, formally defined as the square root of the ratio of the minimum and maximum eigenvalues of the inertia matrix, is not just related to its fractal dimension but also to its number of particles N: for the same d_f the elongation increases with N or R_g for the porous Eden growth model [42] (Fig. 12). Secondly, decreasing d_f will also affect the number of bonded contacts within the aggregates as a larger amount of new bonded contacts are formed when increasing the particle radius during the preparation stage (see 4.1.1). The initial coordination number (only bonded contacts, i.e. before tension-compression cycling) goes from 2.7 for $d_f = 1.7$ to 3.5 for $d_f = 2.8$. On the contrary, for $d_f = 2.0$ increasing R_g will not significantly change the initial coordination number. The influence of lowering d_f is thus twofold:

- Because of a more elongated and branched structure, more Hertzian contacts are formed which hinders the reorganizations and tends to increase the compaction stress.

- Aggregates are less stiff because of a lower number of bonded contacts per particles, which tends to decrease the compaction stress.

These two competing effect may compensate each other, and finally lead to the apparent very limited influence of d_f on compaction noted on Fig. 11. On the contrary, increasing R_g does not affect the initial number of bonded contacts and the compaction stress is governed only by the amount of

Hertzian contacts which increases with R_g leading to the expected behavior: more elongated aggregates are more difficult to compact.

The observed relatively weak influence of γ_s on the compaction behavior is not consistent with recent experimental results. Indeed, moderate ageing of FS has a significant effect on the compaction behavior [25] that is attributed to a decrease of surface energy (gain of hydrophilicity [13]). The simulations have two possible bias that might explain the inconsistency with experiments:

- increasing amount of geometrical bond breakages with increasing surface energy may lead to an artificially too soft compaction behavior;
- preparation by compression-tension cycling was done with $\gamma_s = 1.2$ J/m^2 for all samples, which may lead to an unrealistically large number of Hertzian contacts, at the beginning of the compaction, for low γ_s and hinder the reorganization.

When focusing on tensile behavior, the effect of surface energy predominates. The oedometric modulus and tensile strength are influenced, in our simulation, by order of significance, by:

- surface energy (or primary particle radius)
- neck size between bonded primary particles
- the aggregate morphology (R_g for E_0 and d_f for σ_f)

The parametric study shows that contact law parameters (neck size a and surface energy γ_s) impact more the mechanical behavior (compaction and post-compaction) than the morphology of the aggregates (fractal dimension

d_f and gyration radius R_g). However the transposition of this result to real silica powder systems is delicate because of the model nature of the numerical aggregates, the omission of larger scale structures (agglomerate and powder grain) and the absence of reliable values for surface energy and neck size. Still, higher surface energy is expected for FS because of its less hydrophilic surface, and neck size might be influenced by the process. The possibly large influence of these last two parameters on the mechanical behavior of silica powders could thus significantly contribute to the stronger mechanical behavior of FS. More insight is provided by the comparison of FS and PS numerically generated according to morphological parameters extracted from SAXS data [11, 25]. It is observed in Fig. 14 that the compaction and tensile behavior of FS and PS are close if only morphological differences are considered (in absence of reliable values, the neck size and surface energy are kept similar for both silicas in the simulations). Morphological differences, i.e. larger aggregate radius of gyration, lower fractal dimension and smaller primary particles of FS, taken alone do not explain completely the experimentally observed large differences in mechanical behavior between FS and PS. In terms of stiffness for example, Fig. 15 shows that morphological differences account for a FS slightly stiffer than PS but experimental instrumented indentation data around 10% density have shown that FS is actually twice stiffer than PS [16]. The stronger behavior of FS in compaction and the higher strength of its compact are thus attributed to a combined effect of morphology of the aggregate, smaller primary particle size, higher surface energy and possibly larger necks between particles. However, the assessment of the significance of each parameter is difficult due to the limitations of the

model and lack of data on surface energies and neck sizes.

In light of these findings, the effect of ageing on the mechanical behavior can be discussed. Hygrothermal ageing has two main effects on nanostructured silica: the decrease of the surface energy through water uptake followed by the growth of the necks between primary particles [13]. It has been clearly shown that these effects are detrimental for thermal insulation [7]. For mechanical behavior, the decrease of surface energy associated with moderate ageing leads to easier powder compaction (formation of less Hertzian contacts leading to easier reorganization). On the contrary, for more severe ageing, the increase of neck size may lead to the reverse. As for the tensile behavior, ageing is expected to decrease the strength as the surface energy is the main factor governing the strength of the compacts.

7. Conclusion

The difference in compaction behavior and post-compaction mechanical properties of a fumed and a precipitated nanostructured silica have been investigated through DEM simulations. A parametric study on a set of morphological parameters (R, d_f and R_g) and simulations on realistic aggregates numerically generated based on SAXS measurements have shown that differences in morphology alone may not explain the experimentally observed large differences in mechanical behavior between FS and PS. The study of the influence of neck size and surface energy have shown that these two properties have more effect than the aggregate morphology in the simulations. While the compaction behavior is largely influenced by the neck size, the surface energy is the first governing parameter for strength. The extension of these

results to real systems should however be treated with caution because of the lack of reliable surface energy and neck size values, and the questionable realistic character of the numerical silica (omission of particle size dispersion and large scale structures). In particular, particle size dispersion may not have a negligible influence on mechanical behavior, as is the case for scattering behavior [50]. Even with these limitations in mind, it is believed that the stronger mechanical behavior of FS as compared to PS is, at least partially, a consequence of larger neck sizes and surface energy. While it is clear that FS have a larger surface energy than PS, it has never been proposed, to our knowledge, that FS may have larger necks. In practice, it may thus be efficient to increase surface energy of PS to improve their mechanical behavior. Increasing the neck size may also improve the mechanical properties but is detrimental for thermal properties [7]. Future research on PS should thus focus not only on adjusting the morphology (e.g. by attempting to decrease their fractal dimension) but also on surface modifications to decrease the hydrophilicity and increase the surface energy as it should be highly beneficial for mechanical properties. An experimental investigation of the effect adsorbed water on surface energy and mechanical behavior of silica powders would be of high interest and may help to decouple the morphological and surface energy effects. The proposed modeling approach could also be improved, for example a more realistic model would include primary particle size dispersion (observed by Benane et al. on FS [11]). Small dispersion on d_f and R_g exists in the present approach but could be enhanced and tuned. The bonded contact law could allow plastic deformation. Indeed, this would solve the issue related to geometrical breakages by relaxing unrealistically

large contact forces. It has been shown that silica glass actually exhibits plasticity when tested at small scales [51, 52].

Acknowledgments

This work was performed within the framework of the Center of Excellence of Multifunctional Architectured Materials, CEMAM AN-10-LABX-44-01 funded by the "Investments for the Future" Program. EDF, French Ministry for Research (CIFRE grant 2014-0903) and MATeB (joint MATEIS EDF RD laboratory) are also acknowledged for their financial support.

References

[1] S. E. Kalnæs, B. P. Jelle, Vacuum insulation panel products: A state-of-the-art review and future research pathways, Applied Energy 116 (2014) 355–375.

[2] H. Simmler, S. Brunner, U. Heinemann, P. Mukhopadhyaya, D. Quénard, H. Sallée, K. Noller, E. Kucukpinar-Niarchos, C. Stramm, M. J. Tenpierik, H. Cauberg, M. Erb, H. Schwab, D. Quénard, E. Kücükpinar-niarchos, C. Stramm, HiPTI - High Performance Thermal Insulation IEA/ECBCS Annex 39. Study on VIP-components and Panels for Service Life Prediction of VIP in Building Applications, Technical Report, 2005.

[3] J. Ã. Fricke, U. Heinemann, H. P. Ebert, Vacuum insulation panels From research to market, Vacuum 82 (2008) 680–690.

[4] M. Alam, H. Singh, S. Suresh, D. Redpath, Energy and economic analysis of Vacuum Insulation Panels (VIPs) used in non-domestic buildings, Applied Energy 188 (2017) 1–8.

[5] P. Johansson, Building Retrofit using Vacuum Insulation Panels, Hygrothermal Performance and Durability, Ph.D. thesis, Chalmers University of Technology, 2014.

[6] S. Q. Zeng, A. Hunt, R. Greif, Transport properties of gas in silica aerogel, Journal of Non-Crystalline Solids 186 (1995) 264–270.

[7] B. Yrieix, B. Morel, E. Pons, VIP service life assessment: Interactions between barrier laminates and core material, and significance of silica core ageing, Energy and Buildings 85 (2014) 617–630.

[8] G. P. Baeza, A. C. Genix, C. Degrandcourt, L. Petitjean, J. Gummel, M. Couty, J. Oberdisse, Multiscale filler structure in simplified industrial nanocomposite silica/SBR systems studied by SAXS and TEM, Macromolecules 46 (2013) 317–329.

[9] P. Karami, N. Al-ayish, K. Gudmundsson, A comparative study of the environmental impact of Swedish residential buildings with vacuum insulation panels, Energy & Buildings 109 (2015) 183–194.

[10] G. Ulrich, Flame synthesis of fine particles, Chem. Eng. News 62 (1984) 22–29.

[11] B. Benane, G. P. Baeza, B. Chal, L. Roiban, S. Meille, C. Olagnon, B. Yrieix, G. Foray, Multiscale structure of super insulation nano-fumed

silicas studied by SAXS , tomography and porosimetry, Acta Materialia 168 (2019) 401–410.

[12] R. Wengeler, F. Wolf, N. Dingenouts, H. Nirschl, Characterizing dispersion and fragmentation of fractal, pyrogenic silica nanoagglomerates by small-angle X-ray scattering, Langmuir 23 (2007) 4148–4154.

[13] B. Chal, B. Yrieix, L. Roiban, K. Masenelli-Varlot, J.-M. Chenal, G. Foray, Nanostructured silica used in super-insulation materials (SIM), hygrothermal ageing followed by sorption characterizations, Energy and Buildings 183 (2019) 626–638.

[14] L. Roiban, G. Foray, Q. Rong, A. Perret, D. Ihiawakrim, K. Masenelli-Varlot, E. Maire, B. Yrieix, Advanced three dimensional characterization of silica-based ultraporous materials, RSC Adv. 6 (2016) 10625–10632.

[15] D. W. Schaefer, C. Chen, Structure optimization in colloidal reinforcing fillers: precipitated silica, Rubber chemistry and technology 75 (2002) 773–794.

[16] B. Benane, S. Meille, G. Foray, B. Yrieix, C. Olagnon, Instrumented Indentation of Super-Insulating Silica Compacts, Materials 12 (2019) 830.

[17] Y. Wang, G. Gu, F. Wei, J. Wu, Fluidization and agglomerate structure of SiO2 nanoparticles, Powder Technology 124 (2002) 152 – 159.

[18] J. C. H. Wong, H. Kaymak, S. Brunner, M. M. Koebel, Mechanical

properties of monolithic silica aerogels made from polyethoxydisiloxanes, Microporous and Mesoporous Materials 183 (2014) 23–29.

[19] T. Woignier, J. Primera, A. Alaoui, P. Etienne, F. Despestis, S. Calas-Etienne, Mechanical Properties and Brittle Behavior of Silica Aerogels, Gels 1 (2015) 256–275.

[20] Q. Liu, Z. Lu, M. Zhu, Z. Yuan, Z. Yang, Z. Hu, J. Li, Simulation of the tensile properties of silica aerogels: the effects of cluster structure and primary particle size., Soft matter 10 (2014) 6266–77.

[21] C. a. Ferreiro-Rangel, L. D. Gelb, Investigation of the bulk modulus of silica aerogel using molecular dynamics simulations of a coarse-grained model., The journal of physical chemistry. B 117 (2013) 7095–105.

[22] W. Gonçalves, J. Morthomas, P. Chantrenne, M. Perez, G. Foray, C. L. Martin, W. Goncalves, J. Morthomas, P. Chantrenne, M. Perez, C. L. Martin, Elasticity and strength of silica aerogels: a Molecular Dynamics study on large volumes, Acta Materialia 145 (2018) 165–174.

[23] W. Gonçalves, J. Amodeo, J. Morthomas, P. Chantrenne, M. Perez, G. G. Foray, C. L. Martin, Nanocompression of secondary particles of silica aerogel, Scripta Materialia 157 (2018) 157–161.

[24] S. P. Patil, A. Rege, M. Itskov, B. Markert, Mechanics of nanostructured porous silica aerogel resulting from molecular dynamics simulations, The Journal of Physical Chemistry B 121 (2017) 5660–5668.

[25] B. Benane, Mécanique des lits de silices granulaires pour l'optimisation

des cœurs de panneaux isolants sous vide (PIV), Ph.D. thesis, INSA de Lyon, 2018.

[26] L. T. Zhuravlev, The surface chemistry of amorphous silica. Zhuravlev model, Colloids and Surfaces A: Physicochemical and Engineering Aspects 173 (2000) 1–38.

[27] M. L. Hair, W. Hertl, Adsorption on hydroxylated silica surfaces, Journal of Physical Chemistry 73 (1969) 4269–4276.

[28] Evonik Industries AG, Aerosil - Fumed Silica: Technical Overview, Technical Report, 2015.

[29] A. P. Legrand, The surface properties of silicas, Wiley, 1998.

[30] P. A. Cundall, O. D. L. Strack, A discrete numerical model for granular assemblies, Geotechnique 29 (1979) 47–65.

[31] D. Potyondy, P. Cundall, A bonded-particle model for rock, International Journal of Rock Mechanics and Mining Sciences 41 (2004) 1329–1364.

[32] C. Kloss, C. Goniva, A. Hager, S. Amberger, S. Pirker, Models , algorithms and validation for opensource DEM and CFD-DEM, Pcfd 12 (2012) 140–152.

[33] A. Stukowski, Visualization and analysis of atomistic simulation data with OVITO the Open Visualization Tool Visualization and analysis of atomistic simulation data with OVITO the Open Visualization

Tool, Modelling and Simulation in Materials Science and Engineering 18 (2010) 015012.

[34] I. Agnolin, J.-N. Roux, Internal states of model isotropic granular packings. I. Assembling process, geometry, and contact networks, Physical Review E 76 (2007) 061302.

[35] J. Christoffersen, M. M. Mehrabadi, S. Nemat-Nasser, A Micromechanical Description of Granular Material Behavior, Journal of Applied Mechanics 48 (1981) 339–344.

[36] C. L. Martin, D. Bouvard, S. Shima, Study of particle rearrangement during powder compaction by the Discrete Element Method, Journal of the Mechanics and Physics of Solids 51 (2003) 667–693.

[37] C. L. Martin, R. K. Bordia, Influence of adhesion and friction on the geometry of packings of spherical particles, Physical Review E 77 (2008) 31307.

[38] B. V. Derjaguin, V. M. Muller, Y. P. Toporov, Effect of contact deformations on the adhesion of particles, Journal of Colloid and Interface Science 53 (1975) 314–326.

[39] G. Jefferson, G. K. Haritos, R. M. McMeeking, G. Je, G. K. Haritos, R. M. Mcmeeking, The elastic response of a cohesive aggregate–a discrete element model with coupled particle interaction, Journal of the Mechanics and Physics of Solids 50 (2002) 2539–2575.

[40] D. Jauffrès, C. L. Martin, A. Lichtner, R. K. Bordia, Simulation of the

elastic properties of porous ceramics with realistic microstructure, Modelling and Simulation in Materials Science and Engineering 20 (2012) 045009.

[41] R. M. McMeeking, G. Jefferson, G. K. Harritos, Elastic and Visco-elastic response of finite particle junctions in granular materials, in: A. Zavalianglos A;Laptev (Ed.), Recent developments in computer modeling of powder metallurgy processes, IOS Press, Amsterdam, 2001, pp. 50–62.

[42] E. Guesnet, R. Dendievel, D. Jauffrès, C. Martin, B. Yrieix, A growth model for the generation of particle aggregates with tunable fractal dimension, Physica A: Statistical Mechanics and its Applications (2017).

[43] K. L. Johnson, K. Kendall, A. D. Roberts, Surface energy and the contact of elastic solids, Proceedings of The Royal Society A 324 (1971) 301–313.

[44] P. Nikolopoulos, S. Agathopoulos, A. Tsoga, A method for the calculation of interfacial energies in AI203 and ZrO2/liquid-metal and liquid-alloy systems, J. Mater. Sci. 29 (1994) 4393–4398.

[45] W. Gonçalves, J. Morthomas, P. Chantrenne, M. Perez, G. Foray, C. L. Martin, Molecular dynamics simulations of amorphous silica surface properties with truncated Coulomb interactions, Journal of Non-Crystalline Solids 447 (2016) 1–8.

[46] B. Morel, L. Autissier, D. Autissier, D. Lemordant, B. Yrieix, D. Que-

nard, Pyrogenic silica ageing under humid atmosphere, Powder Technology 190 (2009) 225–229.

[47] K.-T. Wan, D. T. Smitht, B. R. Lawn, Fracture and Contact Adhesion Energies of Mica-Mica, Silica-Silica, and Mica-Silica Interfaces in dry and moist atmospheres, Journal of the American Ceramic Society 3 (1992) 667–676.

[48] T. A. Michalske, E. R. Fuller, Closure and Repropagation of Healed Cracks in Silicate Glass, journal of the am 68 (1985) 586–590.

[49] L. J. Gibson, M. F. Ashby, Cellular solids. Structure and properties 2nd Ed., Cambridge University Press, 1997.

[50] A.-C. Genix, J. Oberdisse, Determination of the local density of polydisperse nanoparticle assemblies, Soft Matter 13 (2017) 8144–8155.

[51] R. Lacroix, G. Kermouche, J. Teisseire, E. Barthel, Plastic deformation and residual stresses in amorphous silica pillars under uniaxial loading, Acta Materialia 60 (2012) 5555–5566.

[52] J. Luo, J. Wang, E. Bitzek, J. Y. Huang, H. Zheng, L. Tong, Q. Yang, J. Li, S. X. Mao, Size-Dependent Brittle-to-Ductile Transition in Silica Glass Nanofibers, Nano Letters 16 (2016) 105–113.